The Effect of Particle Size and Morphology on the In-Flight Behavior of Particles during High-Velocity Oxyfuel Thermal Spraying

D. CHENG, Q. XU, G. TRAPAGA, and E.J. LAVERNIA

A one-way coupled mathematical model is formulated to simulate the effects of particle size and morphology on the momentum and thermal energy transfer of particles during high-velocity oxyfuel (HVOF) thermal spraying. First, computational fluid dynamic techniques are implemented to solve the Favre-averaged mass, momentum, and energy conservation equations in the gas phase. The gas dynamic data are then used to model the behavior of particles in the gas field. The concept of sphericity is used to incorporate the effect of particle morphology into the model. The calculated results show that the particle velocity and temperature, before impinging onto the substrate, are strongly affected by particle size, morphology, and spray distance. Smaller particles are accelerated to a higher velocity but slowed down rapidly due to their smaller momentum inertia, while the larger particles are accelerated with some difficulty. The same tendency is observed regarding the effect of particle size on its thermal history.

I. INTRODUCTION

HIGH-VELOCITY oxyfuel (HVOF) thermal spraying is one of the most significant developments in the thermal-spray industry since the development of the original plasma spray technique. It is being used in an increasing variety of coating applications. Metallic, ceramic, and composite coatings are frequently applied to substrates to improve wear resistance, abrasion resistance, thermal and electrical barriers, and corrosion protection.[1] More recently, HVOF thermal spraying has been successfully used as a means of producing nanocrystalline coatings.[2–7] The extremely brief exposure of the precursor nanocrystalline particles to the high temperatures of the HVOF process appears to preserve the nanocyrstalline structure in most of the particles deposited on the substrate. The HVOF is characterized by high particle velocities and relatively low thermal energy when compared to plasma spraying. The HVOF uses an internal combustion jet fuel (propylene, acetylene, propane, and hydrogen gases) to produce a gas temperature greater than 3029 K[8] and to generate a supersonic or hypersonic gas velocity of approximately 2000 m/s, more than 5 times the speed of sound, through a convergent-divergent nozzle. The powder particles are injected into the gas jet, and simultaneously heated, and propelled toward the substrate. With the relatively low temperature of the flame gas associated with the HVOF system, as compared to plasma spraying (about 15,000 K),[9] the particles are made highly plastic by convective heat transfer, and superheating or vaporization of individual particles is prevented.[10] Furthermore, low particle temperatures experienced during the deposition of carbide coatings lead to less carbide depletion than plasma-sprayed coatings. In effect, the advantages of HVOF over conventional plasma spraying include higher coating bond strength, higher deposition rate, higher hardness, lower oxide content, and improved wear resistance due to a homogeneous distribution of particles.[11,12]

From the fluid dynamics point of view, the system is very complex and involves two-phase (gas and liquid or solid particles) flow with turbulence, heat transfer, chemical reaction, and supersonic/subsonic flow transitions. In an engineering application, the microstructure and physical properties of the coatings are determined by the physical and chemical properties of the particles impinging on the substrates, which in turn are dependent on a large number of parameters such as gun design, the fuel/oxygen ratio, the gas jet formation, the position of substrate relative to the gun, the particle size, shape, materials, injection method, and so on. Hence, to successfully apply the HVOF technique, it is necessary to optimize all of these parameters.

In the past few years, computational fluid dynamic methods have been used to provide insight into the complex flow behavior during HVOF thermal spraying.[14–19] However, available investigations have concentrated on the flame gas dynamics and particles with a spherical geometry due to the distinct advantages both in numerical and experimental studies.[17,18,19] While in many cases, such as nanocrystalline powders prepared by mechanical milling, the geometry of the particle is nonspherical, the effect of particle geometry on the particle behavior during HVOF has never been studied.

In this article, a one-way coupled model is used to simulate the gas and particle dynamics. First, computational fluid dynamic techniques are implemented to solve the mass, momentum, and energy conservation equations of the gases. The results of gas dynamics are then used to calculate the temperature and velocity of particles during flight. The effect

D. CHENG, formerly Graduate Student, Department of Chemical and Biochemical Engineering and Materials Science, University of California, Irvine, is Research Engineer, Pace Enterprises, Los Angeles, CA 90013. Q. XU, Research Engineer, and E.J. LAVERNIA, Professor and Chair, are with the Department of Chemical and Biochemical Engineering and Materials Science, University of California, Irvine, CA 92697. G. TRAPAGA, formerly Principal Research Associate, Department of Materials Science and Engineering, Massachusetts Institute of Technology, Cambridge, MA 02139, is Professor, Laboratorio de Investigacion en Materiales del CINVESTAV-IPM, Unidad Queretaro, Fracc. Real de Juriquilla, C.P. 76230, Qro., Mexico.

Manuscript submitted March 8, 2000.

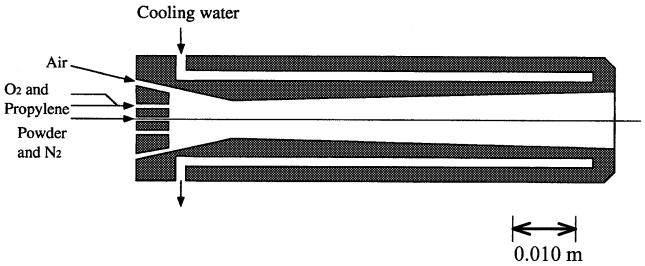

Fig. 1—Geometry of the convergent-divergent HVOF gun used in the present study.

of morphology is incorporated into the model by addressing the concepts of sphericity and projected area. The objective of the article is to provide a fundamental understanding of the effects of size and morphology of feedstock powders on the heat and momentum transfer between the flame and particles.

II. GUN GEOMETRY

A Sulzer-Metco Diamond Jet gun (Sulzer Metco Inc., Westbury, NY) is used in the present research. Figure 1 shows a schematic sketch of its inner geometry. A convergent-divergent nozzle is designed to generate a supersonic jet. A fuel gas is premixed with oxygen in a proprietary siphon system in the front portion of the gun. The thoroughly mixed gases are then ejected from the annular gap to the convergent-divergent nozzle and externally ignited. The exhaust gases, along with the compressed air injected from the annular inlet orifice, form a circular flame configuration that surrounds powder particles input from the central inlet hole. This circular flame shapes the powder stream to provide uniform heating and melting. Heated powder particles are accelerated by a high velocity flow of the exhaust gases. Finally, the high velocity particles impact upon a substrate to form a dense, hard, and well-bonded coating.

III. NUMERICAL FORMULATION

Since the particle loading in HVOF is very low (less than $1/10^6$), it can be assumed that the presence of particles will have a negligible effect on the gas velocity and temperature field in the barrel and in the free jet. This allows the governing equations for gases and particles to be described separately. Furthermore, since the number of particles in the unit volume is small, it can also be assumed that the particles are collisionless in the flow. As a result of these assumptions, the two-phase problem can then be coupled in only one way, and one can simulate the gas flow first and then use the resulting thermal and velocity fields to study the flow of different particles through the established flow pattern.

A. *Gas Dynamics*

The gas flow during HVOF thermal spraying is governed by three general conservation equations of mass, momentum, and energy.[20,21,22] Turbulent flows are inherently unsteady and contain a wide range of time and length scales, and resolution of these scales requires very short time-steps and fine grids. The CPU and memory requirements are too large even for the fastest and largest present day computers. As we are more interested in time-mean quantities, in the present study, the Favre (or density) approach[23] is used to average the conservation equations. In the average process, a flow quantity ϕ is decomposed into mean and fluctuating parts. The following two types of averaging are used.

Reynolds (or time) averaging:

$$\phi = \overline{\phi} + \phi' \quad \text{where} \quad \overline{\phi} = \left(\frac{1}{\Delta t}\right)\int_{t0}^{t0+\Delta t} \phi dt \qquad [1]$$

Favre (or density ρ) averaging:

$$\phi = \tilde{\phi} + \phi'' \quad \text{where} \quad \tilde{\phi} = \overline{\rho\phi}/\overline{\rho} \qquad [2]$$

Note that the overbar denotes Reynolds averaging, while the tilde denotes Favre averaging.

Applying the Favre averaging, mass conservation can be expressed as

$$\frac{\partial \overline{\rho}}{\partial t} + \frac{\partial}{\partial x_j}(\overline{\rho}\tilde{u}_j) = 0 \qquad [3]$$

where u_j is the jth Cartesian component of the instantaneous gas velocity. The repeated indices imply summation over all coordinate directions. The Favre-averaged momentum conservation equation is

$$\frac{\partial}{\partial t}(\overline{\rho}\tilde{u}_i) + \frac{\partial}{\partial x_j}(\overline{\rho}\tilde{u}_i\tilde{u}_j) = -\frac{\partial \overline{p}}{\partial x_i} + \frac{\partial}{\partial x_j}\left[\overline{\mu}\left(\frac{\partial \tilde{u}_i}{\partial x_j} + \frac{\partial \tilde{u}_j}{\partial x_i} - \frac{2}{3}\frac{\partial \tilde{u}_k}{\partial x_k}\delta_{ij}\right)\right] + \frac{\partial}{\partial x_j}(-\overline{\rho}u_i''u_j'') \qquad [4]$$

where p is the static pressure, μ the viscosity coefficient, and δ_{ij} the Kronecker delta. The Fave-averaged energy conservation equation is

$$\frac{\partial}{\partial t}(\overline{\rho}\tilde{H}) + \frac{\partial}{\partial x_j}(\overline{\rho}\tilde{u}_i\tilde{H}) = \frac{\partial}{\partial x_j}\left(k\frac{\partial \tilde{T}}{\partial x_j}\right) + \frac{\partial \tilde{p}}{\partial t} + \frac{\partial}{\partial x_j}\left[\overline{\mu}\left(\frac{\partial \tilde{u}_i}{\partial x_j} + \frac{\partial \tilde{u}_j}{\partial x_i} - \frac{2}{3}\frac{\partial \tilde{u}_k}{\partial x_k}\delta_{ij}\right)\right] - \frac{\partial}{\partial x_j}(\overline{J}_{ij}\overline{h}_i) + \overline{S}_a \qquad [5]$$

where H is the total enthalpy, κ the conductivity, J_{ij} the total diffusive mass flux, h_i the enthalpy for species i, and S_a the additional sources.

The Favre-averaging process introduces unknown terms called the Reynolds stresses $\overline{\rho}u_i''u_j''$, as shown in Eq. [4]. The Boussinesq eddy viscosity concept[24] is employed to treat these stresses. The renormalization group (RNG) κ-ε model[25] is applied to estimate the turbulent eddy viscosity. Standard semiempirical wall functions[24] are used in the cells adjacent to walls to represent turbulence boundary conditions.

B. *Combustion*

Hydrocarbon combustion is a very complex process that may consist of a great number of elementary reactions, currently not fully understood for this type of system. At high temperatures, dissociation of product species takes place due to strong thermal atomic vibration. A chemical reaction between a hydrocarbon and oxygen often does not go to completion and create stable products according to a simple

stoichiometric equilibrium at room temperature. Moreover, the kinetics of all elementary reactions and the dissociation of species are time dependent, and related to local pressure, temperature, and species concentrations. These complexities, along with the size and speed limitations of computers, make it very difficult to numerically simulate the detailed reaction kinetic mechanisms of a combustion process. Thus, some simplifying assumptions become necessary in order to render the problem tractable. In the present research, an approximate formulation that takes into account the effect of dissociation is used to treat the gas combustion process:

$$C_3H_6 + 3.552O_2 \rightarrow 1.036CO_2 + 1.964CO + 0.441H + 0.476H_2 + 1.937H_2O + 0.3980 + 0.734OH \quad [6]$$

This formulation was suggested by Oberkampf and Talpallikar[26] according to the One-Dimensional Equilibrium Chemistry code developed by Gorden and McBride.[27] In the following calculations, an instantaneous chemistry model is used to implement the preceding combustion formulation. In all calculations, propylene and oxygen are assumed to react immediately upon contact, that is, the reaction rate is infinitely rapid. In the present study, the equivalence ratio of propylene and oxygen within the overall injected stream is

$$\phi = \frac{f_{\text{propylene}}/f_{\text{oxygen}}}{(f_{\text{propylene}}/f_{\text{oxygen}})_{\text{stoichiometric}}} = 1.15 \quad [7]$$

where f is the mass fraction of fuel or oxidant. The overall injected stream is set to be fuel rich in order to minimize the oxidation extent of sprayed powder particles and to achieve a high flame temperature.

C. *Momentum Transfer of Powder Particles*

Upon entering the gun chamber with the carrier gas, powder particles are accelerated or decelerated due to the velocity difference with the exhaust gases. The motion of the particles is governed by Newton's law, which describes the balance of forces acting on a particle and which can be written as

$$m_p \frac{d\mathbf{V}_p}{dt} = \sum \mathbf{F} = \mathbf{F}_D + \mathbf{F}_G \quad [8]$$

In the case of HVOF, the force of gravity, $\mathbf{F}_G = m_p\mathbf{g}$ can be neglected because the drag force, $\mathbf{F}_D$, represents, by far, the most significant term in the balance equation. Thus, Eq. [8] can be written as

$$m_p \frac{d\mathbf{V}_p}{dt} = \mathbf{F}_D = \frac{1}{2}\rho A_{pn} C_D (\mathbf{V} - \mathbf{V}_p)|\mathbf{V} - \mathbf{V}_p| \quad [9]$$

where m_p, V_p, A_{pn}, and V_p are the mass, volume, projected area, and velocity of a particle, and $\mathbf{V}$ is the velocity of the exhaust gas. Different standard expressions of the drag coefficient, C_D, specific for spherical particles, have been proposed to represent gas-particle interactions. However, no theoretical or experimental studies have addressed the drag behavior of nonspherical particles in HVOF systems. Several groups such as Haider and Levenspiel,[28] Thompson and Clark,[29] and Ganser[30] have attempted to develop universally applicable drag expressions for two-phase flows (particle-gas). Among them, Ganser's model is believed to be able to provide the most accurate prediction of particle velocities.[31] In this study, the Ganser model is used to incorporate the effect of particle morphology. Ganser's analysis hinges on the fact that every particle experiences a Stoke's regime, where the drag is linear in velocity, and a Newton's regime, where the drag is proportional to the square of velocity. He thus introduced two shape factors, K_1 and K_2, applicable in the Stokes' and Newton's regimes, respectively, and derived the following drag correlation:

Table I. Expressions for K_1 and K_2 in Terms of the Sphericity Index ψ[30]

Shape	K_1	K_2
Isometric	$[(1/3) + (2/3)\psi^{-0.5}]^{-1}$	$10^{1.8148(-\log\psi)^{0.5743}}$
Nonisometric	$[(d_n/3d) + (2/3)\psi^{-0.5}]^{-1}$	$10^{1.8148(-\log\psi)^{0.5743}}$

Notes: d is sphere diameter or equal volume sphere diameter (m) and d_n the equal projected area diameter (m).

$$\frac{C_D}{K_2} = \frac{24}{\text{Re}K_1K_2}[1 + 0.1118(\text{Re}K_1K_2)^{0.6567}] + \frac{0.4305}{1 + \frac{3305}{\text{Re}K_1K_2}} \quad [10]$$

where C_D and Re are based on the equal volume sphere diameter, and K_1 and K_2 are unique functions of the particle sphericity index, ψ, as shown in Table I. Particle sphericity is a particle-shape index defined as the ratio of surface area of a sphere of equivalent volume divided by the surface area of the particle.

To precisely predict the momentum transfer between the gas phase and particles, it is necessary to consider the effect of gas turbulence. Up to now, however, the expressions of C_D for nonspherical particles are merely based on experiments, and no experimental data could be found concerning the drag correlation in turbulent flow for nonspherical particles. Therefore, in this article, the effect of gas turbulence on the particle trajectories is ignored.

D. *Heat Transfer of Powder Particles*

For thermal spraying, the sizes of powder particles often are several tens of microns. Because the Biot number (B_i) is typically less than 0.1, any temperature gradient within these particles may be conveniently neglected. Therefore, a Newtonian heating-cooling approach is assumed to represent particle heat transfer, which can be expressed as

$$m_p c_p \frac{dT_p}{dt} + Q_m = k_h A_p (T_w - T_p) + \varepsilon\sigma(T^4 - T_p^4) \quad [11]$$

where c_p is the specific heat of the powder material, σ the Stephen–Boltzmann constant, and ε surface emissivity. The heat source term, Q_m, is originated from the phase transformation at the melting point and can be expressed as

$$Q_m = \Delta H_m \frac{dm_{\text{pl}}}{dt} \quad [12]$$

where m_{pl} is the mass of liquid fraction of a particle and ΔH_m the latent heat of fusion of the particle.

As with the drag correlation, the effect of nonsphericity

on heat transfer is very complex.[32] In this study, the heat-transfer coefficient, k_h, in Eq. [11] is grossly estimated using the Ranz and Marshall correlation:[33]

$$k_h = \frac{K_g}{d}\,(2 + 0.6\mathrm{Re}^{1/2}\mathrm{Pr}^{1/3}) \qquad [13]$$

where K_g is the thermal conductivity of gas, d is the equal volume sphere diameter of a particle, and Pr is the gas Prandtl number.

IV. NUMERICAL SOLUTION

A. *Gas phase*

The present calculations for gas phase dynamics and combustion are implemented using the commercial package CFD-ACE+. Because the gun geometry is symmetrical about its axis, a one-half, two-dimensional grid is used to simulate the gas phase flow behavior. The grid is finer in the regions where large gradients of flow properties exist, and gradually changes to be coarser in the regions where small gradients of flow properties are expected. Two computational domains are used to define the gas flow inside and outside the gun. The computational domain inside the gun contains 2697 cells (control volumes). The computational domain outside the gun is 0.254-m (10 in., the practical spraying distance) long and 0.05-m wide, and contains 8849 cells. In prescribing boundary conditions, the pressure and temperature in the inlets of the inside domain are adjusted to satisfy the mass flow rate conditions typically used in our experimental system. All of the solid walls of the nozzle are assumed at a uniform temperature of 1000 K. This value was selected, by trial and error, in order to satisfy the experimental data of energy losses in the gun. A constant pressure condition is used at the outlets of the outside domain (1 atm). An adiabatic thermal condition is assumed at the substrate. Thermophysical properties for the mixture of gases used in the calculations were taken from the JANAF tables.[36]

The Favre-averaged mass, momentum, and energy conservation equations and the turbulence equations are solved using the cell-centered control volume approach, which means that the discretized equations are formulated by evaluating and integrating fluxes across the faces of control volumes in order to satisfy the relevant conservation equations. The discretized equations are formulated by evaluating and integrating fluxes across the faces of the control volumes in order to satisfy the conservation requirements. Each dependent variable is solved at the center of each control volume, and the value obtained is considered to prevail over the entire control volume. The assembled algebraic equations for each dependent variable are solved sequentially and repeatedly. For all solutions presented here, the sum of the residuals for each dependent variable decreases at least five orders of magnitude during iteration so that a convergent solution is obtained. The residual at one control volume is defined as the difference between the values of a dependent variable at the present iteration and the previous iteration.

In the calculation procedure used in the present study, various interpolation schemes with varying levels of numerical accuracy and stability are used to obtain a satisfactory solution. An upwind scheme,[34] which is first order in accuracy and the most stable, is at first used to obtain a converged solution. Then, using that solution as an initial guess, a third-order Osher–Chakravarthy scheme[35] is used to capture shock waves possibly occurring during HVOF thermal spraying. All the following calculations use a relative pressure convention, and the reference pressure is set at 10^5 Pa.

Table II. Physical Properties of WC-18Co[36,37,38]

Density, kg/m^3	14,600
Melting temperature of WC, K	3073
Melting temperature of Co, K	1765
Latent heat of fusion of Co, J/kg	2.63×10^5
Surface emissivity	0.40
Specific heat, J/kg K	$246 + 0.078T_p - 4.22 \times 10^{-6}\,T_p^{-2}$ ($289\ \mathrm{K} < T_p < 650\ \mathrm{K}$) $224 + 0.107T_p - 3.96 \times 10^{-6}\,T_p^{-2}$ ($650\ \mathrm{K} < T_p < 1400\ \mathrm{K}$) $300 + 0.037T_p - 3.96 \times 10^{-6}\,T_p^{-2}$ ($T_p > 1400\ \mathrm{K}$)

B. *Particles*

After the mass, momentum, and energy conservation equations of the gases are solved by computational fluid dynamic techniques, the gas dynamics data are used to solve particle momentum and heat-transfer equations. The numerical solution of Eqs. [9] and [11] is carried out using an explicit program in which the drag coefficient correlation, Eq. [10], is implemented.

WC-18Co, which consists of 82 wt pct tungsten carbide and 18 wt pct cobalt, is chosen as a model particle material. The relevant material properties are shown in Table II, which were taken from references in the literature.[36,37,38] Since there are limited data for WC-18Co in the literature, some properties are estimated from the data of WC and Co.

V. MODEL VALIDATION

Typical HVOF devices use supersonic flow conditions at their nozzle exit, in order to transfer as much kinetic energy to the powder as possible. As the exit pressure of a converging-diverging nozzle depends strongly on the combination of inlet temperature and pressure, in most cases, the static pressure at the barrel exit does not match the ambient atmospheric pressure. In these cases, a repetitive sequence of expansion and compression waves will be generated in the free jet. During the expansion, the Mach number increases and the temperature and pressure decrease; during compression, the reverse occurs. The highest gas temperature is reached after compression waves. As some gaseous species luminesce at high temperatures, these areas can be seen and are usually termed “shock diamonds.”

An essential factor of the theoretical supersonic turbulence model is its ability to describe the variations of the gas dynamic characteristics along the jet centerline or diamond shocks. This capability is strongly influenced by the model formulation and the solution technique. However, experimental measurements on gas flow characteristics, such as pressure, temperature, or velocity distribution, are limited, particularly for the case of HVOF systems. Thus, to partially

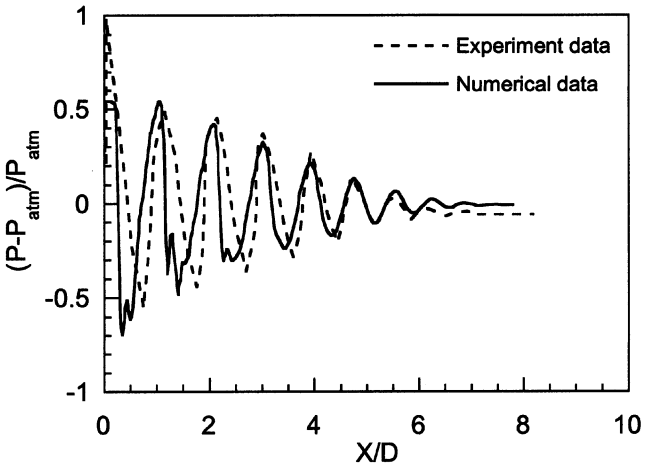

Fig. 2—Comparison of numerical and experimental results for the gas pressure along the centerline of a nozzle operating at Mach 2. Conditions at the nozzle exit are nozzle diameter, 0.05 m; gas pressure, 54,000 Pa; and gas flow velocity, 22.7 mol/s.

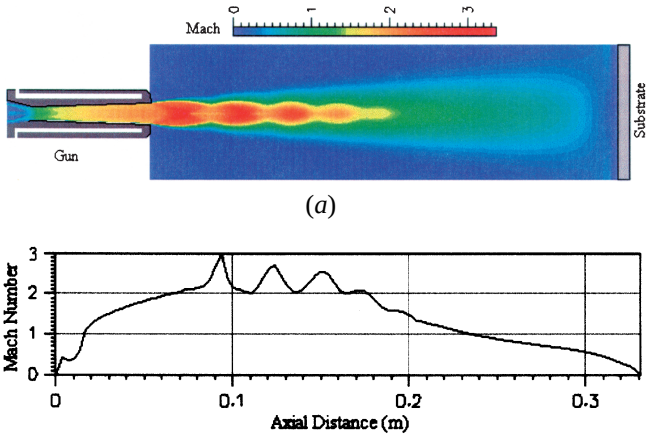

Fig. 3—(*a*) Predicted flooded Mach number contour over the calculation domain and (*b*) Mach number profiles along the centerline. Gas flow rates: propylene, 6.2 × 10^{-5} mol/s; oxygen, 20.3 × 10^{-5} mol/s; nitrogen, 0.99 × 10^{-5} mol/s; and cooling air, 30.2 × 10^{-5} mol/s.

validate the numerical model used in the present study, it has been used to simulate an underexpanded Mach 2 nozzle expanding into still air, for which Seiner and Norum have measured the gage pressure change along the centerline.[39] Figure 2 shows the comparison of numerical and experimental results. In Figure 2, *X* is the distance from the nozzle exit while *D* is the nozzle diameter at the exit. It can be seen that both the intensity and position of shock waves agree very well with the experimental result, demonstrating the strong capabilities of the present model.

VI. NUMERICAL RESULTS

A. *Gas Dynamics*

Since the scope of the present article is to investigate particle size and morphology effect, only illustrative results of gas dynamic for a typical experimental condition are presented.

Figure 3 shows (a) the field of Mach number (M) contours

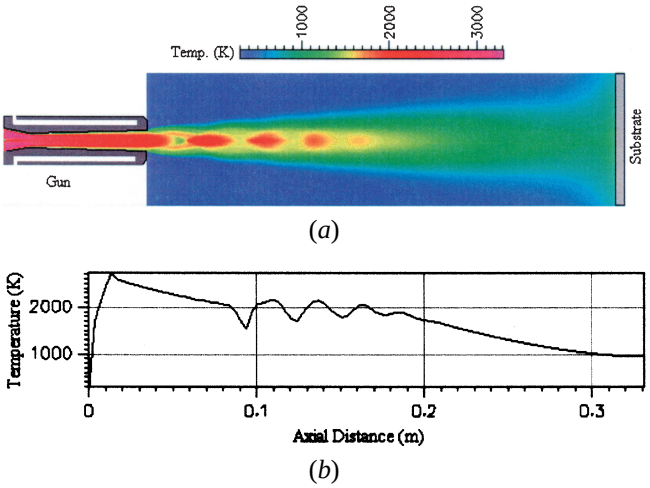

Fig. 4—(*a*) Predicted flooded contours of gas temperature over the entire computational domain and (*b*) temperature profile along the centerline. Gas flow rates: propylene, 6.2 × 10^{-5} mol/s; oxygen, 20.3 × 10^{-5} mol/s; nitrogen, 0.99 × 10^{-5} mol/s; and cooling air, 30.2 × 10^{-5} mol/s.

over the entire calculation domain, together with (b) the Mach number profile along the centerline. In Figure 3, the gas inlet position is represented by an axial distance of zero. In the convergent portion of the nozzle, the velocity of the gas mixture is low, but is then accelerated to approximately M = 1 at the nozzle throat (axial distance equals 0.016 m). In the divergent portion, the gas is further accelerated to a supersonic velocity, and reaches M = 2.1 (V = 2032 m/s) at the nozzle exit. At this location, the calculated gas pressure is about 41 kPa (above ambient pressure). Therefore, the gas flow is underexpanded and can be further accelerated during expansion to a highest velocity of 2530 m/s. Upon leaving the nozzle, the gas mixture is accelerated and decelerated repetitively due to expansions and compressions, and decays to a subsonic velocity after several cycles. Following this cyclic behavior, the gas velocity constantly decreases due to dissipation of energy of the viscous flow.

The gas temperature contours, over the entire computational domain, together with the temperature profile along the centerline, are shown in Figures 4(a) and (b), respectively. The figure shows that the gas temperature is highest along the path of the fuel and oxidant, in the convergent portion of the gun. This is a natural result of the instantaneous chemistry model with the assumption that the reaction proceeds as soon as the gas enters the nozzle. The highest temperature in the flow field is about 3200 K, which is consistent with calculations made by Hassan *et al.* using a one-dimensional equilibrium model.[15] The cooling effects imposed through the boundary conditions can be seen along the inner gun walls. Four diamond shocks are also predicted as regions of elevated temperature outside the nozzle. The temperature of the gases increases rapidly in the convergent portion as a result of the combustion reactions and reaches the highest value near the nozzle throat. In the divergent region of the gun, the temperature continuously decreases as a result of the energy transfer to kinetic energy. Beyond the exit of the gun, the repetitive expansion and compression cycles cause temperature fluctuations, apparent by the four shock diamonds. The characteristic shape of the shock diamonds agrees well with experimental observations made as part of this study and is the result of the repeated reflections

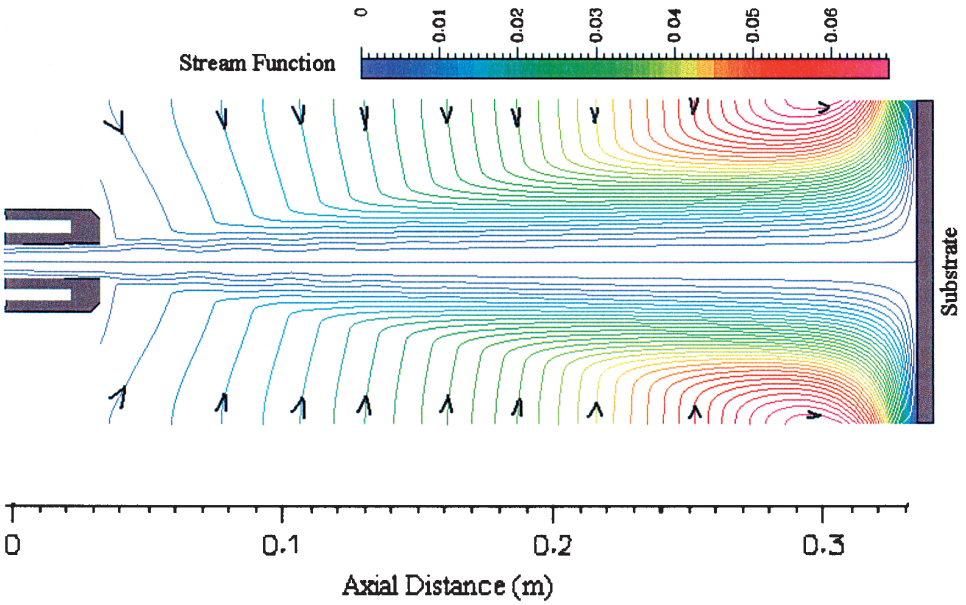

Fig. 5—Calculated streamlines of the gas phase. Gas flow rates: propylene, 6.2×10^{-5} mol/s; oxygen, 20.3×10^{-5} mol/s; nitrogen, 0.99×10^{-5} mol/s; and cooling air, 30.2×10^{-5} mol/s.

of oblique pressure waves within the supersonic core of the jet as the gas flow expands and compresses in an attempt to reach an equilibrium with the surrounding atmosphere. Upon exiting the nozzle, the flow first expands and its temperature drops, and thus visible-light emission ceases. The jet tends to overshoot the ambient pressure condition, and a subsequent compression region raises the gas temperature and renders it visible once again. This pattern of expansion and compression waves is repeated until mixing with the surrounding atmosphere eventually dissipates the supersonic jet. Entrainment of secondary air can be clearly seen in the calculated streamlines shown in Figure 5. Stream function is a scalar function of the space coordinates only and is constant along a streamline.[40] The entrainment of secondary air is so strong that a bulk airflow is induced in the vicinity of the HVOF jet along the axial direction toward the substrate. This calculated phenomenon agrees well with the experimental observation by Hackett *et al.*[41] with a full-field Schlieren imaging technique.

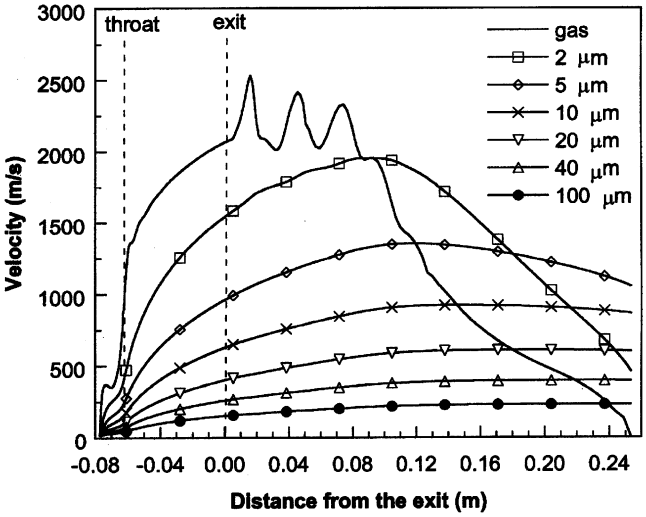

Fig. 6—Predicted axial velocities of spherical particles with different diameters as a function of distance from the gun exit. Gas flow rates: propylene, 6.2×10^{-5} mol/s; oxygen, 20.3×10^{-5} mol/s; nitrogen, 0.99×10^{-5} mol/s; and cooling air, 30.2×10^{-5} mol/s.

B. *The Effect of Particle Size*

Figure 6 shows the predicted axial velocities of particles with different diameters during flight. The gas velocity is also shown in the same figure for comparison. Upon entering the nozzle, the particles are accelerated by the gas in the combustion chamber. It is evident from Figure 6 that the particle size has a strong effect on the particle acceleration and deceleration behavior during their entire trajectories. Smaller particles are easily accelerated to a much higher velocity because of their smaller inertia. The particle velocity increases until the point where its speed equals that of the surrounding gas. Therefore, a small particle starts to slow down at a shorter distance from the exit, *e.g.*, 0.1 m for particles with a diameter of 2 μm, while larger particles are accelerated for a longer distance. As a result of air entrainment, the gas slows down rapidly after a distance of 0.1 m from the exit and the smallest particles can attain the highest maximum velocity during flight. This does not imply, however, that the smallest particles can have higher velocities upon arrival to the substrate surface since they are also decelerated earliest and more rapidly. For example, a 2-μm particles can obtain a maximum velocity as high as 2740 m/s, but its velocity at the typical spraying distance of 0.254 m (10 in.) is only 457 m/s. While the highest velocity of a 20-μm particle is 607 m/s, its velocity at the same spraying distance is 598 m/s, still higher than that of 2-μm particles.

The axial velocities of particles at the typical spray distance of 0.254 m are shown in Figure 7 as a function of particle size. As seen in the plot, a particle with a diameter of 10 μm has the highest velocity (over 1000 m/s) at this distance. For longer spraying distances, however, larger particles will have higher velocities since the smaller particles

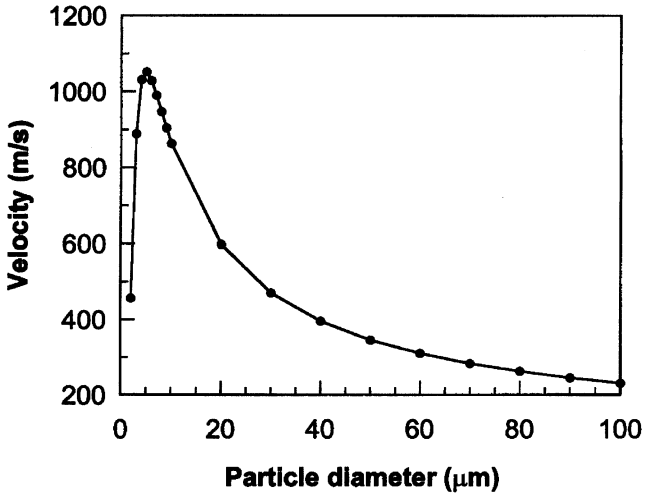

Fig. 7—Predicted effect of particle size on its axial velocity at a spray distance of 0.254 m. Gas flow rates: propylene, 6.2×10^{-5} mol/s; oxygen, 20.3×10^{-5} mol/s; nitrogen, 0.99×10^{-5} mol/s; and cooling air, 30.2×10^{-5} mol/s.

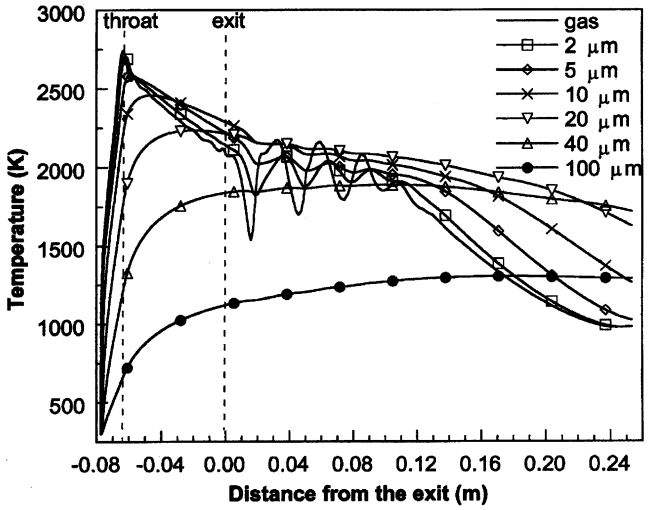

Fig. 8—Predicted temperatures of spherical particles with different diameters as a function of distance from the gun exit for axial flow. Gas flow rates: propylene, 6.2×10^{-5} mol/s; oxygen, 20.3×10^{-5} mol/s; nitrogen, 0.99×10^{-5} mol/s; and cooling air 30.2×10^{-5} mol/s.

are decelerated more rapidly. The results show that for particles between 10 and 60 μm, typically used in thermal spraying applications, particle velocities are in the range between 310 and 860 m/s at a typical spraying distance of 0.254 m. This range of velocities is much higher than the typical velocity of 200 m/s, which can be obtained by plasma spraying.[10,42,43] At this spraying distance, there is a large difference (510 m/s) between the particle velocity for a 10-μm particle and that for a 60-μm particle. This difference in velocities is equivalent to a kinetic energy per unit mass of the impinging particle, which is one order of magnitude different. Of course, this will lead to different deformation conditions as splats are being formed, since it is widely accepted that the higher the velocity, the better the coating quality. The argument is based on the premise that the greater velocity can pack the coating more tightly. Therefore, according to the results shown in Figure 7, particles with a diameter larger than about 30 μm will tend to form more porous coatings due to their decreasingly lower velocity. These results also imply that it would be difficult to obtain high-quality coating when the particle size is too small (*e.g.*, 2 μm) since its velocity is also low at the spray distance considered. Therefore, the results confirm the importance of controlling the size of the feedstock powders in order to obtain the desired coating quality. It is also worth noticing that the velocities of particles larger than 20 μm do not vary greatly with distance from the gun exit, a characteristic which makes it easier to control the deposition parameters.

Figure 8 shows the predicted temperature of particles for six different particle diameters at the jet's centerline. As can be seen in the figure, the 2- and 5-μm particles follow closely the gas temperature. These small particles reach the local gas temperature before entering the divergent portion inside the gun and continuously cool down with the decreasing gas temperature. As cold ambient air is entrained and cools the gas jet drastically, the particle temperature drops rapidly as well. Beyond a distance of 0.24 m from the nozzle exit, the temperature of a 2-μm particles equals the gas temperature. The particles with diameters of 10 and 20 μm reach the gas temperature inside the convergent portion of the nozzle,

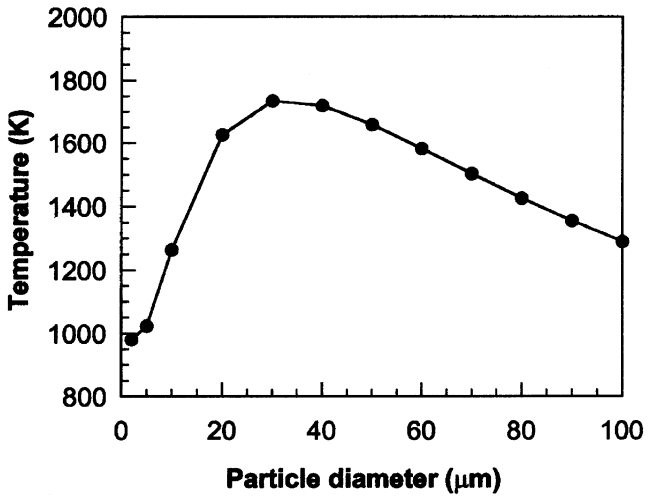

Fig. 9—Predicted effect of particle size on its temperature at a spray distance of 0.254 m. Gas flow rates: propylene, 6.2×10^{-5} mol/s; oxygen, 20.3×10^{-5} mol/s; nitrogen, 0.99×10^{-5} mol/s; and cooling air 30.2×10^{-5} mol/s.

and after exiting the gun nozzle, the particle temperatures decrease monotonically. The temperatures for particles larger than 20 μm reach the gas temperature after exiting the gun nozzle due to the high thermal inertia of the large particles. These 10- to 20-μm particles also cool down slowly when the gas temperature is below the particle temperature. From Figure 8, the temperature of particles larger than 20 μm remains relatively unchanged upon exiting the gun up to a distance of 0.25 m. The temperature of a particle, at a certain spray distance, depends strongly on its size, similar to the previously discussed trends for particle velocities. This trend is illustrated in Figure 9. At a spray distance of 0.254 m, the 30-μm particle has the highest temperature. Therefore, at this distance, particles of approximately 30 μm will have optimal thermal energy for the particle to spread during impingement. Although smaller particles have higher maximum temperature before impinging the substrate, their cooling rate is faster due to their smaller thermal inertia. With

an increase in spraying distance, the maximum temperature at the spraying distance will shift to larger particles due to the difference in the thermal inertia. However, the maximum temperature will decrease with an increase in spraying distance.

From the point of view of a larger operational window, particles larger than 20 μm appear to yield optimal results in terms of temperature control and uniformity.

A high temperature prior to substrate impingement is beneficial to coating quality since the impinging particles are readily deformed, thereby leading to a high coating density. Nevertheless, a high-temperature exposure during flight does not necessarily render a better coating. For example, in the case of WC-Co coatings, the thermal history of the particle prior to impingement may also lead to undesirable effects, such as the dissolution of WC in Co and decarburization of particles by secondary air. According to the Co-C[44] phase diagram, the maximum solubility of C atoms in solid-state Co is 0.9 wt pct at 1593 K and increases to 5 wt pct at 2073 K (the melting point temperature of Co is 1768 K). A high solubility of W atoms in Co can be seen in the W-Co[45] phase diagram, *i.e.*, Co can dissolve 39.8 wt pct W at the melting point temperature of Co. In HVOF processes, the flame temperature may not be enough to decompose WC directly, but certainly can do so through the dissolution of WC into the Co binder. In related work, it was reported that large amounts of W and C dissolved into a Co matrix during thermal spraying.[46,47] Furthermore, it was reported that the higher the maximum temperature the powder experienced, the more severe the dissolution that occurred in the coating.[48] From Figure 8, it can be seen that small particles, especially those with a diameter equal to or less than 20 μm, experience higher temperature than larger particles. It can be predicted that coating made from smaller particles will have more severe dissolution relative to one made of large particles. Moreover, when the particle temperature is high, the periphery of the semimolten particle becomes easier to decarburize by the oxygen in the secondary air,[49,50] which means that small particles are less likely to obtain a high-quality coating, since for a certain volume of powders, there will be more surface area for small particles than for large particles.

In the preparation of nanocrystalline coatings, it is critical to prevent grain growth since it is precisely the small grain size that contributes to the unique properties of the materials. Therefore, it is important to keep a relatively high particle temperature at the spraying position while simultaneously preventing the particle from overheating during flight. For particles smaller than 10 μm, the maximum temperature that they experience is in the range 2400 to 2700 K, while the temperature at the spraying distance is less than 1300 K. Therefore, the use of particles smaller than 10 μm is not recommended.

C. *The Effect of Morphology*

From a modeling standpoint, it is more challenging to study nonspherical particles than spheres because of the influence of particle orientation. In this study, to investigate the effect of morphology, oblate spheroidal particles with the same equal volume diameter (30 μm) but different aspect ratio E (the ratio of short axis to long axis, b/a) were considered. Spheroidal particles are chosen because it is easy to calculate the surface area, volume, and sphericity, and they allow the study of shapes ranging from slightly deformed spheres to disks. Results for thin disks can be obtained in the limit as E approaches zero. Moreover, oblate spheroids with different E represent a good approximation for the wide range of powders prepared by mechanical milling.

Table III. The Relationship between Geometric Characteristics of Spherically Oblate Particles*

Aspect Ratio E (b/a)	$2a/d$	$2b/d$	Sphericity (ψ)
1	1	1	1
0.5	1.26	0.63	0.913
0.4	1.36	0.54	0.85
0.3	1.49	0.45	0.76
0.2	1.71	0.34	0.63
0.1	2.15	0.22	0.42
0.05	2.71	0.14	0.27
0.01	4.64	0.046	0.093

*The axial dimension of the particle is $2b$; and the maximum dimension normal to the axis of symmetry is $2a$. The equal sphere diameter is d.

In this model, it is assumed that the particle does not change its shape above the melting temperature of the binding metal phase Co, as long as it is below the melting point of WC. This is reasonable considering the results of Lau *et al.*,[3] in which the geometry of INCONEL* 718 flakes does not change their shapes significantly after going through the spray system, though their melting point (1533 to 1608 K) is lower that of Co (1765 K). After reaching the melting point of WC, however, we assume that all geometry will change into spherical shape.

*INCONEL is a trademark of INCO Alloys International, Huntington, WV.

For nonspherical particles, the momentum transfer between particles and fluid depends strongly on orientation during flight, which in turn depends on the Reynolds number. Therefore, it is essential to correctly choose the particle direction in the simulation of in-flight behavior of nonspherical particles. In the case of HVOF processes, the Reynolds number of the particles is usually less than 500. In this Re regime, the particles usually align themselves with their maximum cross section normal to the direction of relative motion.[51,52,53] Therefore, it is reasonable to assume that the symmetry axis (shorter axis, b) aligns with the direction of motion. Table III provides a summary of the geometric parameters for the particles used in the present study. All the particles have the same equal volume diameter of 30 μm.

Figure 10 shows the predicted axial velocities of oblate particles with different aspect ratios, E, as a function of distance from the powder injection point. The velocities of particles with $E = 0.5$ and 0.4 are not shown because they are very close to that of the spherical particle ($E = 1$), which is also included in the plot. This indicates that when the aspect ratio is larger than 0.4 (corresponding to a sphericity value greater than 0.85), the dynamic behavior of those particles is very similar to that of spherical particles. However, with decreasing aspect ratios, the particle velocity increases, relative to spherical particles. Figure 11 shows the predicted axial velocities of particles with different aspects

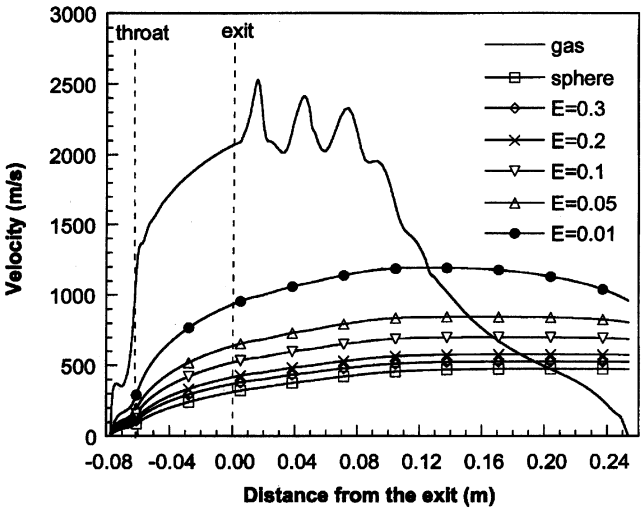

Fig. 10—Predicted velocities of oblate particles with different aspect ratios, *E*, as a function of distance from the gun exit. All particles have the same equal volume diameter of 30 μm. Gas flow rates: propylene, 6.2×10^{-5} mol/s; oxygen, 20.3×10^{-5} mol/s; nitrogen, 0.99×10^{-5} mol/s; and cooling air, 30.2×10^{-5} mol/s.

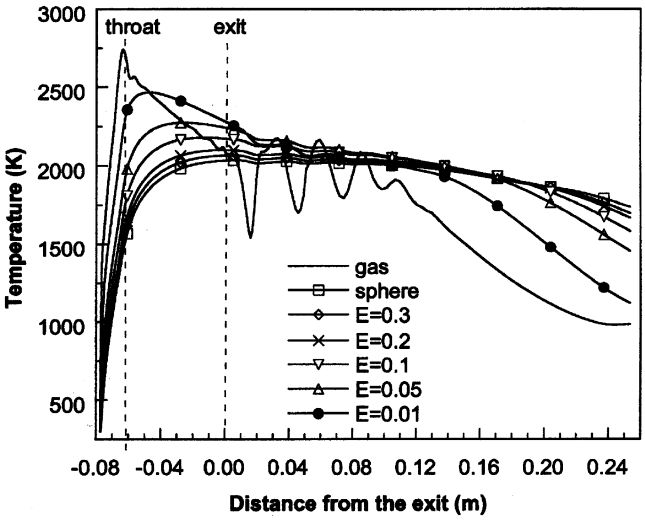

Fig. 12—Predicted temperatures of oblate particles with different aspect ratios, *E*, as a function of distance from the gun exit. All particles have the same equal volume diameter of 30 μm. Gas flow rates: propylene, 6.2×10^{-5} mol/s; oxygen, 20.3×10^{-5} mol/s; nitrogen, 0.99×10^{-5} mol/s; and cooling air, 30.2×10^{-5} mol/s.

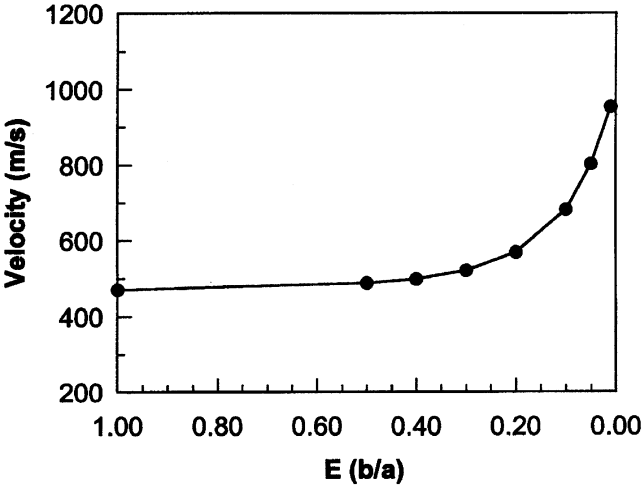

Fig. 11—Predicted effect of the aspect ratio, *E*, on the velocity of the oblate particle at a spray distance of 0.254 m. All particles have the same equal volume diameter of 30 μm. Gas flow rates: propylene, 6.2×10^{-5} mol/s; oxygen, 20.3×10^{-5} mol/s; nitrogen, 0.99×10^{-5} mol/s; and cooling air, 30.2×10^{-5} mol/s.

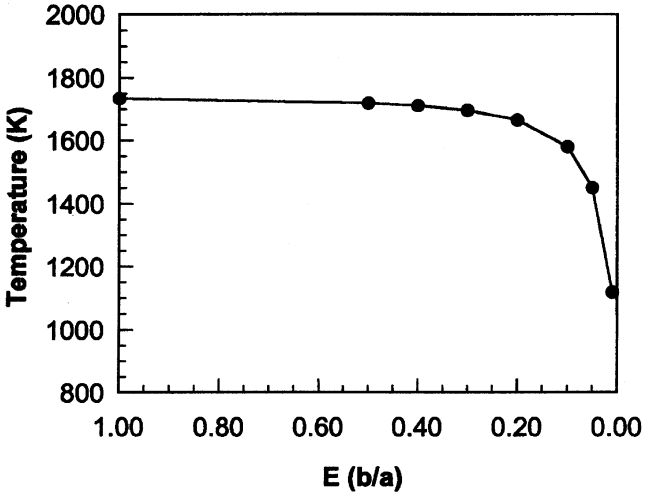

Fig. 13—Predicted effect of the aspect ratio, *E*, on the temperature of the oblate particle at a spray distance of 0.254 m. All particles have the same equal volume diameter of 30 μm. Gas flow rates: propylene, 6.2×10^{-5} mol/s; oxygen, 20.3×10^{-5} mol/s; nitrogen, 0.99×10^{-5} mol/s; and cooling air, 30.2×10^{-5} mol/s.

ratios at the spray distance of 0.254 m. For particles with aspect ratios larger than $E = 0.5$, the particle velocity remains relatively unchanged. Beyond that value of *E*, the velocity increases continuously with a decrease in the value of *E*. For a particle with $E = 0.01$, the velocity is as high as 954 m/s, approximately 2 times that of an equivalent spherical particle.

The increase of velocity is beneficial for coating quality. However, it is not the only factor affecting coating quality. The effect of morphology on the particle temperature is shown in Figure 12. Again, the temperatures for particles with $E = 0.5$ and 0.4 are not included in the figure since they are close to that of spherical particles. When the value of *E* is smaller than 0.4, the particle temperature obviously differs from that of a spherical particle. The smaller the value of *E*, the more rapidly the particle heats or cools. This is because the rate of heat transfer is enhanced by the increase in particle surface area, as shown by Eq. [11]. As the value of *E* decreases, the sphericity decreases and the surface area increases; hence, the rate of heat transfer also increases. For the particle with $E = 0.01$, the particle experiences a maximum temperature of 2467 K, compared to a value of 2035 K for a spherical particle with the same volume. However, the temperature of the particle at the spray distance is only 1120 K, considerably lower than 1734 K for the spherical particle. Figure 13 shows the variation of temperature of oblate particles as a function of the aspect ratio at a spraying distance of 0.254 m. It is clear from the figure that smaller aspect ratios result in decreasing particle temperatures. From a practical point of view, the effect of lower

particle temperatures prior to impingement on the coating quality may be considered negative since this would limit the extent of deformation of splats and thereby would lead to a low density. Simultaneously, the higher maximum temperature associated with particles corresponding to $E < 0.3$ may also lead to decarburization and grain growth during flight, as discussed previously.

Therefore, the influence of morphology on particle velocity and temperature yields opposite trends in terms of coating quality. On the basis of the results described in the present article, it appears logical to suggest that in the case of nanostructured coatings, a decrease in spray distance is desirable. It is also evident, however, that the overall effect of particle morphology on the coating quality needs to be clarified *via* well-coordinated theoretical and experimental studies.

VII. CONCLUDING REMARKS

In this article, we presented computed results describing momentum and heat-transfer interactions between spherical and nonspherical powder particles and the mixture of combustion gases generated by an HVOF system. The mathematical model implemented in this study allows for an appropriate representation of compressibility effects in the flow, combustion, turbulence, and *ad-hoc* correlations to include the effect of particle morphology.

Particular attention was given to partially validate the theoretical fluid model in order to guarantee a satisfactory representation of the inherent supersonic and turbulence characteristics in HVOF systems. Since experimental measurements are rather limited in HVOF, a comparison of results for a supersonic air jet, for which data are available in the literature, was used to indirectly validate the model. This comparison showed an excellent agreement. The model was also capable of accurately capturing the supersonic diamond shocks observed in HVOF experiments under identical operating conditions.

The importance of the numerical model formulated herein lies in its ability to provide insight into the behavior of irregular particles during HVOF thermal spraying; irregular particle morphologies have become increasingly important with the advent of nanostructured coatings, which involve arrays of agglomerates, disks, and other nonspherical morphologies. The principal areas of uncertainty remaining include an improved understanding of the specific role of particle velocity *vs* temperature during the process of splat formation, particularly in cases of nonspherical particles.

The principal findings of the work may be summarized as follows.

1. The results of the model predict that the HVOF device can generate a supersonic flame with a high velocity and high temperature. The flame is slowed and cooled rapidly after several repetitive expansion and compression waves after exiting the nozzle.
2. At the typical spray distance of 0.254 m, the 10-μm particles have the highest velocity. Smaller particles are accelerated to a higher velocity during flight but slowed rapidly due to their smaller momentum inertia, while the larger particles find a limited acceleration response. At longer distance, however, larger particles will tend to reach higher velocities.
3. At the spray distance of 0.254 m, the model also predicts that 30-μm particles have the highest temperature. Smaller particles are heated to a higher temperature but are cooled rapidly due to their smaller thermal inertia, while the larger particles are heated with difficulty. As suggested by the results, at longer spray distance, larger particles would experience maximum temperatures.
4. For oblate spheroids, the aspect ratio E has little effect on particle velocity and temperature when its value exceeds 0.4. However, when the aspect ratio decreases further, the particle velocity increases with the temperature. When $E = 0.01$, particle velocities may be 2 times higher, while their temperature may be 700 K lower than the corresponding values for spherical particles with the same volume.

ACKNOWLEDGMENTS

The authors thank the reviewers of this paper for many helpful suggestions. The authors acknowledge the financial support of the Office of Naval Research under Grant Nos. N00014-94-1-0017 and N00014-98-1-0569. The authors also thank Yaojun Lin for many helpful discussions.

NOMENCLATURE

a	long semiaxis of a spheroidal particle (m)
A_p	surface area of a particle (m^2)
A_{pn}	projected area of a particle on the plane perpendicular to the flow (m^2)
b	short semiaxis of a spheroidal particle (m)
B_i	Boit number, defined as $k_a d/k_h$
c_g	specific heat of gas (J/kg K)
c_p	specific heat of the powder material (J/kg K)
C_D	drag coefficient
d	sphere diameter or equal volume sphere diameter (m)
D	nozzle diameter at the exit (m)
d_n	equal projected area diameter (m)
E	aspect ratio of a spheroidal particle
f	the mass fractions of fuel and oxidant
H	total enthalpy of gas (J/kg)
h_i	enthalpy for species i (J/kg)
J_{ij}	total diffusive mass flux (kg/m^2 s)
k_h	heat-transfer coefficient of a particle (J/m K)
k_a	mean coefficient of heat transfer between a particle and gas (J/m^2 K)
K_1, K_2	shape factors in low and high Reynolds number regions, respectively
K_g	the thermal conductivity of gas (W/m K)
M	Mach number
m_p	mass of a particle (kg)
m_{pl}	mass of liquid fraction of a particle (kg)
p	static pressure (Pa)
Pr	gas Prandtl number, defined as $\mu c_g/k$
Re	Reynold number, defined as $\rho\lvert\mathbf{V}\text{-}\mathbf{V}_p\rvert d/\mu$
S_a	additional sources (J/s)
t	time (s)
t_0	starting time
Δt	a period of time (s)
T	temperature of flame gas (K)
T_p	temperature of a particle (K)
$\mathbf{V}$	velocity of the flame gas (m/s)

V_p	volume of a particle (m^3)
$\mathbf{V}_p$	velocity of a particle (m/s)
X	distance from the nozzle exit (m)
ρ	gas density (kg/m^3)
ψ	particle sphericity index
u_j	jth Cartesian component of the instantaneous gas velocity
μ	viscosity coefficient of gas ($N\ s/m^2$)
δ_{ij}	Kronecker delta
ΔH_m	latent heat of fusion of a particle (J/kg)
σ	Stephen–Boltzmann constant (5.66×10^{-8})
ε	surface emissivity

REFERENCES

1. D.W. Parker and G.L. Kutner: *Adv. Mater. Processing*, 1991, vol. 140, p. 68.
2. B.H. Kear and P.R. Strutt: *Naval Res. Rev.*, 1995, vol. 4, p. 4.
3. V.L. Tellkamp, M.L. Lau, A. Fabel, and E.J. Lavernia: *Nanostruct. Mater.*, 1997, vol. 9, pp. 489-92.
4. B.H. Kear and G. Skandan: *Nanostruct. Mater.*, 1996, vol. 7, p. 913.
5. H.G. Jiang, M.L. Lau, and E.J. Lavernia: *Nanostruct. Mater.*, 1998, vol. 10, pp. 168-78.
6. M.L. Lau, V.V. Gupta, and E.J. Lavernia: *Nanostruct. Mater.*, 1998, vol. 10, pp. 715-22.
7. M.L. Lau, H.G. Jiang, W. Nuchter, and E.J. Lavernia: *Solidi Status Phys.*, 1998, pp. 257-68.
8. L. Pawlowski: *The Science and Engineering of Thermal Spray Copatings*, John Wiley & Sons, Chichester, United Kingdom, 1995.
9. R.B. Heimann: *Plasma-Spray Coating: Principles and Applications*, VCH Verlagsgesellschaft Mbh, New York, NY, 1996, p. 19.
10. D.J. Varacalle, M.G. Ortiz, C.S. Miller, T.J. Steeper, A.J. Rotolico, J. Nerz, and W.L.R. Riggs: in *Thermal Spray: International Advances in Coatings Technology*, C.C. Berndt, ed., ASM INTERNATIONAL, Materials Park, OH, 1992, pp. 181-87.
11. T.S. Srivatsan and E.J. Lavernia: *J. Mater. Sci.*, 1992, vol. 27, pp. 5965-78.
12. D. Apelian, D. Wei, and B. Farouk: *Metall. Mater. Trans. B*, 1989, vol. 20B, pp. 251-62.
13. W.D. Swank, J.R. Fincke, D.C. Haggard, and G. Irons: *Proc. 7th Nat. Thermal Spray Conf.*, Boston, MA, June 20–24, 1994, pp. 313-18.
14. W.L. Oberkampf and M. Talpallikar: *J. Thermal Spray Technol.*, 1996, vol. 5, pp. 53-68.
15. B. Hassan, A.R. Lopez, and W.L. Oberkampf: *J. Thermal Spray Technol.*, 1998, vol. 7, pp. 71-77.
16. S. Eidelman, X. Yang, I. Lottati, and W. Grossmann: *Proc. 8th Nat. Thermal Spray Conf.*, Houston, TX, Sept. 11–15, 1995, pp. 219-24.
17. C.H. Chang and R.L. Moore: *J. Thermal Spray Technol.*, 1995, vol. 4, pp. 358-66.
18. X. Yang and S. Eidelman: *J. Thermal Spray Technol.*, 1996, vol. 5, pp. 175-84.
19. V.V. Sobolev, J.M. Guilemany, J.C. Garmier, and J.A. Calero: *Surf. Coating Technol.* 1994, vol. 63, pp. 181-87.
20. F.M. White: *Fluid Mechanics*, McGraw-Hill Book Company, New York, NY, 1979.
21. P.A. Thompson: *Compressible-Fluid Dynamics*, McGraw-Hill Book Company, New York, NY, 1972.
22. A.G. Cambel: *Gas Dynamics*, Dover Publications, Inc., New York, NY, 1968.
23. T. Cebeci and A.M.O. Smith: *Analysis of Turbulent Boundary Layers*, Academic Press, New York, NY, 1974.
24. B.E. Launder and D.B. Spalding: *Comput. Methods Appl. Mech. Eng.*, 1974, vol. 3, p. 269.
25. V. Yakhot, S.A. Orszag, S. Thangam, T.B. Gatski, and C.G. Speziale: *Phys. Fluids*, 1992, vol. 4, pp. 1510-20.
26. W.L. Oberkampf and M. Talpallikar: *Proc. 7th Nat. Thermal Spray Conf.*, Boston, MA, June 20–24, 1994, pp. 381-92.
27. S. Gordon and B.J. McBride: "Computer Program for Calculation of Complex Chemical Equilibrium Compositions, Rocket Performance, Incident and Reflected Shocks, and Chapman-Jonquet Detonations," NASA SP-273, NASA, Cleveland, OH, 1976; new version, 1989.
28. A.M. Haider and O. Levenspiel: *Powder Technol.*, 1989, vol. 58, p. 63.
29. T.L. Thompson and N.N. Clark: *Powder Technol.*, 1991, vol. 67, p. 57.
30. G.H. Ganser: *Powder Technol.*, 1993, vol. 77, p. 143.
31. R.P. Chhabra, L. Agarwal, and N.K. Sinha: *Powder Technol.*, 1999, vol. 101, pp. 288-95.
32. J.K. Comer and C. Kleinstreuer: *Int. J. Heat Mass Transfer*, 1995, vol. 38, p. 3171.
33. W.E. Ranz and W.R. Marshall: *Chem. Eng. Progr.*, 1952, vol. 48, pp. 141-46 and 173-80.
34. C. Hirsch: *Numerical Computation of Internal and External Flows*, Wiley, New York, NY, 1988, vol. 1.
35. S.R. Chakravarthy and S. Oscher: AIAA paper no. 85-0363, AIAA, Reno, Nevada, Jan. 1985.
36. M.W. Chase *et al.*: *JANAF Thermochemical Tables*, 3rd ed., American Chemical Society, Washington DC, and American Institute of Physics for the National Bureau of Standards, New York, NY, 1986.
37. D.R. Lide: *The CRC Chemistry and Physics Handbook*, CRC Press, Ann Arbor, MI, 1995.
38. E.A. Brandes and G.B. Brook: *Smithells Metals Reference Book*, Butterworth-Heinemann, Oxford, United Kingdom, 1992.
39. J.M. Seiner and T.D. Norum: *AIAA 12th Fluid and Plasma Dynamics Conf.*, Williamsburg, VA, July 23–25, 1979, paper no. 79-1526.
40. M.A. Saad: *Compressible Fluid Flow*, Prentice-Hall, Englewood, Cliffs, NJ, 1993, p. 72.
41. C.M. Hackett, G.S. Settles, and J.D. Miller: *J. Thermal Spray Technol.*, 1994, vol. 3, p. 299.
42. M.D. Harvery, A.J. Sturgeon, F.J. Blunt, and S.B. Dunkerton: in *Thermal Spraying: Current Status and Future Trends*, A. Ohmori, ed., High Temperature Society of Japan, ASM International, Materials Park, OH, 1995, pp. 531-35.
43. O. Knotek and U. Schnaut: in *Thermal Spraying: International Advances in Coatings Technology*, C.C. Berdt, ed., ASM INTERNATIONAL, Materials Park, OH, 1992, pp. 811-16.
44. K. Ishida and T. Nishizawa: in *Binary Alloy Phase Diagrams*, 2nd ed., T.B. Massalski, ed., ASM INTERNATIONAL, Materials Park, OH, 1990, p. 836.
45. S.V.N. Naidu, A.M. Sriramamurthy, and P.P. Rao: in *Binary Alloy Phase Diagrams*, 2nd ed., T.B. Massalski, ed., ASM INTERNATIONAL, Materials Park, OH, 1990, p. 1258.
46. A. Karimi, C. Verdon, and G. Barbezat: *Surf. Coating Technol.*, 1993, vol. 57, pp. 13-23.
47. S. Usmani, S. Sampath, and H. Herman: *J. Thermal Spray Technol.*, 1998, vol. 7, pp. 429-31.
48. J. He, M. Ice, S. Dallek, and E.J. Lavernia: *Metall. Mater. Trans. A*, 2000, vol. 31A, pp. 541-53.
49. A. Karimi, C. Verdon, and G. Barbezat: *Surf. Coating Technol.*, 1993, vol. 57, pp. 81-89.
50. D.A. Stewart, P.H. Shipway, and D.G. McCartney: *Acta Mater.*, 2000, vol. 48, pp. 1593-604.
51. W.C. Krumbein: *Trans. Am. Geophys. Union*, 1942, vol. 23, pp. 621-33.
52. W.B. Kunkel: *J. Appl. Phys.*, 1948, vol. 19, pp. 1056-58.
53. R. Clift, J.R. Grace, and M.E. Weber: *Bubbles, Drops, and Particles*, Academic Press, Inc., New York, NY, 1978.